Enhanced Transition-Temperature Reduction in a Half-Sphere Au/VO_2 Core-Shell Structure: Local Plasmonics versus Induced Stress and Percolation Effects

Igal Balin,[1] Shancheng Wang,[2] Peikui Wang,[2] Yi Long,[2,3,*] and Ibrahim Abdulhalim[1,3,†]

[1]*Department of Electro-Optics and Photonics Engineering, Ben-Gurion University of the Negev, Beer Sheva 84105, Israel*

[2]*School of Materials Science and Engineering, Nanyang Technological University, 50 Nanyang Avenue, 639798 Singapore*

[3]*Singapore-HUJ Alliance for Research and Enterprise (SHARE), Nanomaterials for Energy and Energy-Water Nexus (NEW), Campus for Research Excellence and Technological Enterprise (CREATE), 138602 Singapore*

(Received 6 May 2018; revised manuscript received 18 February 2019; published 27 March 2019)

VO_2 undergoes metal-insulator transition (MIT) at the transition temperature (τ_c) of 68 °C, accompanied by a sharp optical response change. A unique Au/VO_2 half-sphere core-shell structure is fabricated to study the temperature-dependent plasmonic effects and the thermochromic response for smart window applications. By increasing the Au core size, the surface plasmonic resonance wavelength of the VO_2 high-temperature rutile phase is tuned from 600 to 720 nm and confirmed by simulations. Meanwhile, τ_c of VO_2 is reduced by up to 10 °C, which is thought to be associated with plasmon-induced or percolation-enhancement-related effects. Modification of τ_c occurs on the optical domain only and not in the electrical domain. The in-depth analysis suggests that the interaction of the plasmon between Au and VO_2 in the near field triggers different mechanisms, which reduce the τ_c of VO_2, in particular under high irradiation levels. However, under normal irradiation levels the main contributing effect is found to be thermal strain at the nanoparticles' surface.

DOI: 10.1103/PhysRevApplied.11.034064

I. INTRODUCTION

Vanadium dioxide (VO_2) is a well-known material due to its first-order metal-insulator transition (MIT) in the vicinity of room temperature (approximately 68 °C, τ_c). When heated beyond the τ_c, VO_2 undergoes a reversible structural reconfiguration from a monoclinic space group ($P2_1/c$) semiconductor phase to a rutile space group ($P4_2/mnm$) metallic phase [1,2]. The MIT results in a decrease in the electrical resistivity by up to four orders of magnitude and an increase in the infrared optical absorption by about one order of magnitude. The modification of optical properties during the MIT make VO_2 an attractive candidate for thermochromic smart window applications [3], all-optical switches [4], tunable metamaterial devices [5], and so on. However, the τ_c of pure bulk VO_2 is too high to be applied specifically for smart window fenestrations.

The commonly employed approach to reduce the τ_c is by doping with metal ions, such as W, Mo, Ti, Mg, and rare-earth elements to the VO_2 lattice [6,7]. However, increasing the doping level in VO_2 films generally leads to either a reduction in the magnitude of the transition or a broadening of the transition width [8,9]. The τ_c has also been shown to be affected by the lattice strain, and it has been demonstrated that strain can be introduced by the careful choice of deposition conditions [10,11]. In addition to thermal excitation, the MIT can be triggered by optical [12] or terahertz [13] pulses, electric fields [14], and charge injection [15].

In recent years, several studies have been published in which the thermochromic response of VO_2 was coupled to metal nanostructures supporting surface plasmons polaritons (SPPs). The plasmonic response of VO_2 has been studied in a beam [16] and scattered nanoparticle form [17]. Great interest has been dedicated to the nanometal-VO_2 composite systems due to their reversibly tunable surface plasmon resonance (SPR) effect and potential applications in temperature-sensitive nanophotonics [18], nanosensors [19], plasmonic switches [20], and so forth. For example, plasmonic switches based on the hybridization between SPPs of silver and VO_2 thin film have been demonstrated, exhibiting very high extinction ratios and moderate insertion losses at short device length [20]. Gold nanoparticles embedded in VO_2 thin film can be used as nanoantennas to probe the MIT [21]. The plasmonic resonance modulation of a single

*LongYi@ntu.edu.sg
†abdulhlm@bgu.ac.il

Au nanoparticle on the VO_2 film has been observed in the visible range at the single-particle level [22]. In terms of the applications in temperature-sensitive devices, nanometal-VO_2 composite structures are supposed to have a large resonance shift (λ_{SPR}) between the semiconductor and metal phases [23]. SPPs can enhance the optically triggered MIT by light-induced Joule heating [24] or by ultrafast injection of hot electrons [25].

Here, we demonstrate the fabrication and characterization of a Au/VO_2 core/shell half-sphere heterostructure. The influence of plasmonic excitation in the Au core on the optical and thermochromic properties of the composite structure is studied experimentally and theoretically. By varying the Au core size, we are able to tune the τ_c of the VO_2 shell in the optical domain. The analysis of the induced thermal strain during the cooling step of the annealing process shows that this could be the dominant reason for τ_c reduction. Percolation-related effects induced by the addition of Au nanoparticles is manifested by conductivity increase without modifying the transition temperature in the electrical domain.

II. EXPERIMENTAL SETUP

A. Materials and methods

Fused silica is used as a substrate for the preparation of the VO_2/Au core/shell structure. Before the gold deposition, the substrates are ultrasonically cleaned by deionized (DI) water and acetone, then purged by a nitrogen air gun. The key preparation procedure is described in Scheme 1. First, the gold is deposited onto the substrate by electron beam evaporation and forms a relatively uniform Au island surface. The island size is controlled by different deposition times: 60, 80, 100, and 120 s. Then, the VO_2 layer is produced by dip coating. The precursor for VO_2 coating is prepared as described in Qian *et al.*'s paper [26]. The vanadium pentoxide powders (300 mg, 99%, Alfa Aesar) are dissolved into the 30% hydrogen peroxide solution (30 ml, 30%, AnalaR NORMAPUR) to form a solution by vigorous stirring at 70 °C. The substrates are immersed for 30 s followed by withdrawing at a constant speed of 120 mm·s^{-1}. Subsequently, the sample is dried in air and annealed in an argon atmosphere at 550 °C for 1 h. The heating and cooling rates are 1 and 3 °C/min, respectively.

B. Simulations

Finite difference time domain (FDTD) simulations are performed using commercial software (FDTD solution, Lumerical Inc., Vancouver, Canada). The optical constants of the materials are selected for operation across the spectral range of 300 to 250 nm [27]. The structure is modeled as a periodic array of Au core/VO_2 shell half spheres placed on a fused silica substrate, the entire system suspended in air/vacuum, and the incident beam modeled as a plane wave propagating along the z axis. To calculate the frequency dependent transmittance, PML (perfectly matched layer) boundary conditions are set for the z direction, and Bloch boundary conditions are applied to the x and y directions of the simulation region. Two-dimensional (2D) frequency domain power monitors are placed at fixed z positions below the structure surface to detect the transmitted beam intensity. Two-dimensional frequency domain field monitors are placed for collection of electric field profiles (at the xz plane) and consequent charge density evaluation at SPR wavelength (at the xy plane). The other parameters are set as follows: a simulation time of 100 fs with an auto-shutoff parameter of 10^{-5}, a mesh accuracy of 5 (i.e., 22 mesh points per wavelength), and mesh refinement algorithm set to "conformal variant 1" allowing for a nonuniform mesh over the FDTD domain.

C. Characterization

The surface topography is determined using AFM (DI-3100, Bruker, Germany) in tapping mode. STEM characterization is performed using a JEOL JEM 2010 with an accelerating voltage of 200 kV. The transmittance spectra in the range of 250–2500 nm is measured with a UV-visible-near-infrared spectrophotometer (Cary 5000, Agilent Ltd) equipped with a Linkam PE120 system Peltier simple heating and cooling stage. The T_{lum} (380–780 nm) and solar transmittance (T_{sol}, 280–2500 nm) are calculated based on the recorded $\%T$ spectra using Eq. (1) [28]. The data reported in this work are the average value of four different sampling points

$$T_{lum/IR/sol} = \frac{\int \varphi_{lum/IR/sol}(\lambda) T(\lambda)\, d\lambda}{\int \varphi_{lum/IR/sol}(\lambda)\, d\lambda}. \quad (1)$$

In the equation, $T(\lambda)$ stands for the spectral transmittance, $\varphi_{lum}(\lambda)$ denotes the standard luminous efficiency function of photopic vision in the wavelength range of 380–780 nm [29], and $\varphi_{IR}(\lambda)$ and $\varphi_{sol}(\lambda)$ represent the IR/solar irradiance spectrum for air mass 1.5 (corresponding to the sun at 37° above the horizon), respectively [30]. Moreover, ΔT_{sol} is calculated as $T_{sol} = T_{sol,20\,^\circ C} - T_{sol,90\,^\circ C}$ [31].

D. Sample designations

The samples are designated using the Au deposition time. S60, S80, S100, and S120 refer to samples with deposition times of 60, 80, 100, and 120 s, respectively.

III. RESULTS AND DISCUSSION

Figures 2(a)–2(d) shows the AFM topography information for the VO_2/Au core-shell composite samples with various Au deposition times. Since other parameters such

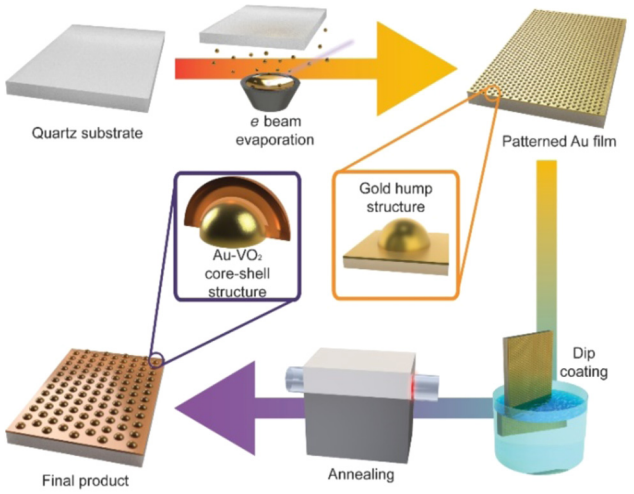

FIG. 1. Schematic diagram of preparation for VO_2/Au half-sphere core-shell structure.

as withdrawal speed and annealing temperature of the growing VO_2 shell are kept constant, the thicknesses of the VO_2 shell are assumed to remain constant. It can also be found that the VO_2/Au core-shell size increases approximately from 40 to 80 nm with increasing deposition time. A STEM image of the core-shell sample (S100) as shown in Fig. 1(e) confirms the geometrically confined VO_2 layer on top of the Au half-sphere structures. The STEM-Energy Dispersive Spectrum (STEM-EDS) compositional maps of V and Au show the geometry of the Au/VO_2 core-shell structure, revealing the individual parts in Figs. 2(f) and 2(g). From Fig. 1(h), it can be seen that the Au half-sphere core diameters vary from 10 to 30 nm.

The transmittance spectra of VO_2/Au samples with various Au deposition times are shown in Fig. 3(a). To explain the regulation effect of SPR, we consider four simple Au nanospheres ranging from 20 to 30 nm in diameter that are coated with 15-nm VO_2 films and simulate the transmission utilizing the FDTD method. The results are demonstrated in the Figs. 3(b) and 3(c) inserted graphs. The solid lines are measured at 20 °C and the dotted lines are measured at 90 °C corresponding to the semiconductor phase and metal phase of VO_2, respectively. All samples exhibit extremely high transmittance contrast between the two phases in the NIR region, which is ascribed to the thermochromic nature of the VO_2 thin film. VO_2 is IR-transparent below τ_c and highly IR-absorptive above τ_c due to the large change of the permittivity induced by phase transition in VO_2. For the case of S60, two extra valleys appear at 630 nm (20 °C) and 600 nm (90 °C) because of the SPR absorption of Au nanoparticles in this visible region. With the increment of the Au core size, two marked phenomena can be observed in the transmittance spectra. First, the plasmonic wavelengths for all the VO_2/Au samples at the semiconductor phase are always larger than those at the metal phase in both experimental and simulation results [Fig. 2(c)]. This phenomenon is related to the change in the dielectric constant of VO_2 during the phase transformation. Second, there is a redshift

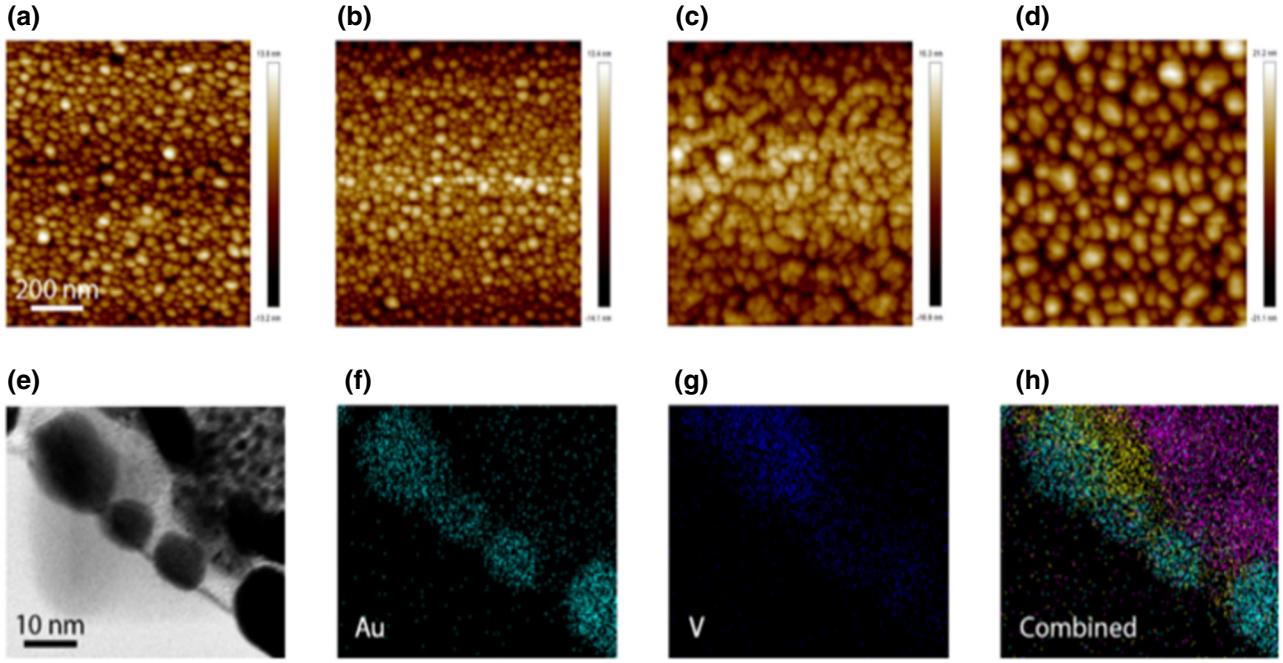

FIG. 2. AFM images of VO_2/Au samples with Au deposition times: (a) 60 s (S60), (b) 80 s (S80), (c) 100 s (S100), and (d) 120 s (S120). (e) TEM image of Au/VO_2 half sphere deposited for 100 s of Au. (f)–(h) STEM element mapping images of Au/VO_2 half sphere deposited for 100 s of Au.

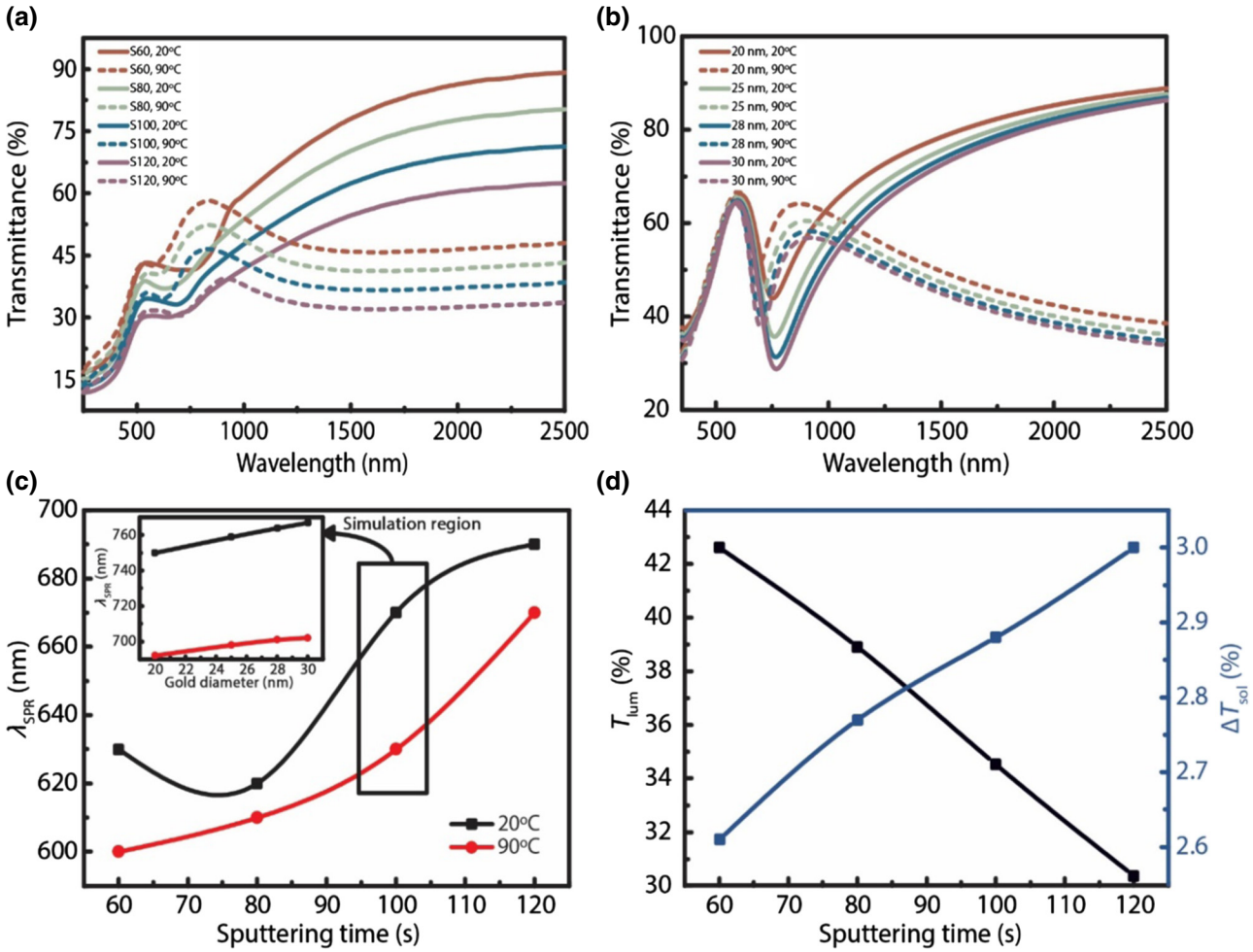

FIG. 3. (a) Transmittance spectra of Au/VO_2 composite with various Au deposition times from 60 to 120 s. (b) Simulation results for Au/VO_2 composite with various Au semisphere diameters of 20, 25, 28, and 30 nm. (c) Values of λ_{SPR} for the samples with different deposition times of Au from 60 to 120 s at 20 °C and 90 °C. The inserted graph is the simulation values of λ_{SPR} for the samples with different Au core diameters. (d) T_{lum} and ΔT_{sol} variation with the deposition time of Au.

of λ_{SPR} especially at higher temperature with increasing Au core size. From Fig. 2(c), the $\lambda_{SPR(90\,°C)}$ increases with the increasing deposition time, which could be due to the gold particles' size. According to the modified Mie theory in quasistatic approximation, the SPR wavelength is linearly dependent on the gold particle radius, which explains the redshift in the SPR wavelength with increasing deposition time [23]. The calculated average values of T_{lum} and ΔT_{sol} for VO_2/Au films varying with the deposition time are shown in Fig. 3(d). It is clear that T_{lum} decreases with the Au amount as a higher amount of Au absorbs more light. Interestingly, ΔT_{sol} increases with the increase of the deposition time since the VO_2 thickness remains unchanged. Possible reasons for this could be due to the redshift of λ_{SPR} in the range of visible light as different wavelength gives different spectral irradiance densities.

The thermal hysteresis loops of VO_2/Au samples measured at 2500 nm and some typical parameters associated with the VO_2 phase transition are shown in Fig. 3. The τ_c is calculated as the averaged τ_c derived from both heating and cooling curves [Fig. 4(a) and inset]. The hysteresis width defines the sharpness of the MIT (the full width at half-maximum of the loop). With the increment of Au deposition time, the value of τ_c decreases from 68.5 °C (S60) to 58 °C (S120) with increasing hysteresis width [Fig. 4(b)]. In the following, we discuss the mechanisms that can explain the reduction of the τ_c, both plasmonic and/or external stresses thermally induced when the metal nanoparticles are incorporated.

A. Plasmonic induced MIT temperature shift

The process by which the electrons will be injected from the gold core to the VO_2 shell can lead to a rise in electron concentration in VO_2, since the work function of Au ($\Phi_{Au} = 4.8$ eV) is lower than that of VO_2

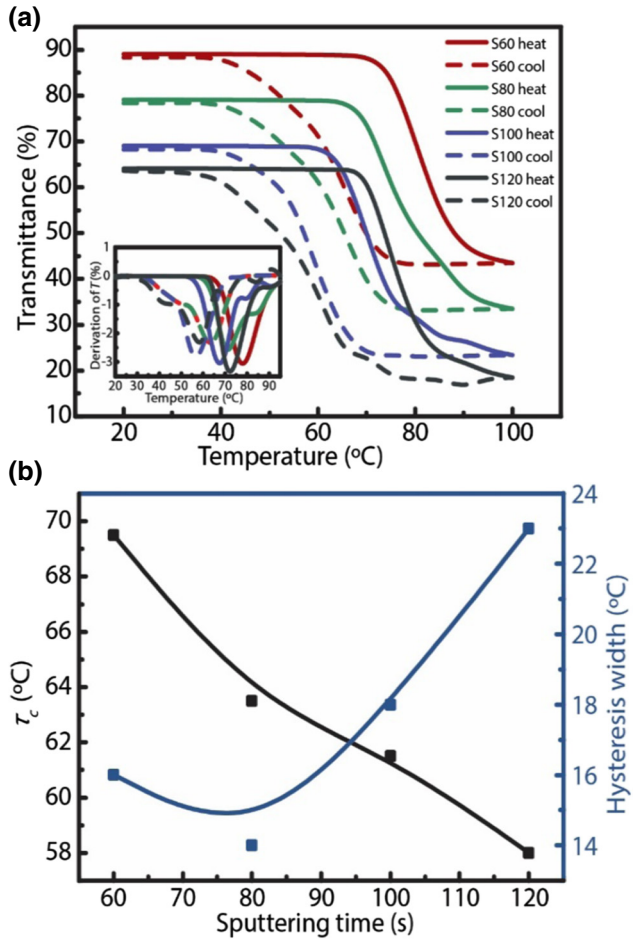

FIG. 4. Thermal hysteresis loops of optical transmittance of VO_2/Au samples with various Au deposition times measured at 2500 nm. The inserted graph is the derivative of transmittance with temperature. (b) The transition temperature and the hysteresis width.

($\Phi_{VO_2} = 5.4$ eV). This explanation is according to the Mott-Hubbard transition whose driving force is electron-electron interaction [32]. However, compared with the previous reports [32–35], our unique core-shell structure provides a higher contact area between Au and VO_2, and the dominant mechanisms that might enhance this effect are worth studying in depth.

The collective resonant oscillation of electrons in plasmonic nanoparticles results in an enhanced local electromagnetic field. Figure 5(a) shows a typical example of the field intensity distribution around a composite of Au/VO_2 half-sphere (core diameter of 28 nm, coating thickness of 15 nm) at the SPR wavelength $\lambda = 0.68$ μm, calculated by the FDTD method. The maximal field intensity enhancement $(E/E_0)^2 \cong 52$ at the Au/VO_2 interface is typical for spherical plasmonic nanoparticles [Figs. 5(a) and 5(c)]. The resonant oscillation of the electron gas of the Au nanoparticle is also responsible for energy dissipation resulting in a potential contribution to the decrease of the Mott MIT temperature of VO_2 by utilizing the three possible mechanisms as follows: (i) the photothermal effect that results in heat generation and consequent temperature increase of the surrounding VO_2 [36], (ii) generation of hot electrons, which can migrate through the Au/VO_2 Schottky junction [25], and (iii) enhanced generation of charge carriers in VO_2 by the local electromagnetic field [Fig. 5(b)]. In the following, we shall estimate the contribution of each one of these mechanisms to the lowering of the τ_c observed experimentally. Although these three mechanisms can occur simultaneously and energy transfer in one of them affects the others, here, we estimate the contribution of each one as if it is independent from the others and the whole energy is independently transferred in one of the mechanisms. A more rigorous model should consider the three mechanisms simultaneously, but this is outside the scope of this paper. The following calculation gives a reasonable estimate of the contribution of each mechanism. The temperature increase as a result of Joule heating can be estimated by solving the heat diffusion equation at steady state conditions. When considering a simple case of a Au spherical nanoparticle surrounded by VO_2, the temperature increase at the Au/VO_2 interface is given by Eq. (2) [37]

$$\Delta T_{\max}(I_0) = \left\{ \mathrm{Re}\frac{R_{\mathrm{AuNP}}^2}{3k_{VO_2}} i\omega[1-\varepsilon_{\mathrm{Au}}(\omega)] \times \left| \frac{3\varepsilon_{VO_2}(\omega)}{2\varepsilon_{VO_2}(\omega)+\varepsilon_{\mathrm{Au}}(\omega)} \right|^2 \frac{I_0}{c\sqrt{\varepsilon_{VO_2}(\omega)}} \right\}, \quad (2)$$

where R_{AuNP} is the Au nanoparticle (AuNP) radius, $k_{VO_2} = 3.5$ W·m^{-1} K^{-1} is the thermal conductivity coefficient of VO_2 in the semiconducting phase, $\varepsilon_{\mathrm{Au}}(\omega)$ and $\varepsilon_{VO_2}(\omega)$ are the frequency-dependent dielectric permittivities of gold and VO_2, respectively, c is the speed of light in vacuum, and I_0 is incident light irradiance. Figure 4(d) shows the wavelength-dependent temperature enhancement for a AuNP that is 28 nm in diameter calculated using air mass (AM) 1.5 solar spectra for incident light irradiance.

To produce an order of magnitude, a 28-nm diameter AuNP surrounded by VO_2 illuminated at resonance wavelength $\lambda = 0.68$ μm with a solar light whose irradiance is $I = 1.2$ W/m^2 experiences a temperature increase of approximately $2{\cdot}10^{-8}$ °C. Consequently, the contribution of Joule heating to the overall Mott transition is negligible.

The conductivity of VO_2 is n type, that is, electrons mainly contribute to the transition and the mobility of charges does not change at the transition [38], therefore, the whole of the conductivity jump is due to the change in charge carrier density. When a Au nanoparticle comes in contact with VO_2, the equilibration of Fermi levels causes the bending of the valence and conduction bands of VO_2 at the interface and a Schottky barrier is

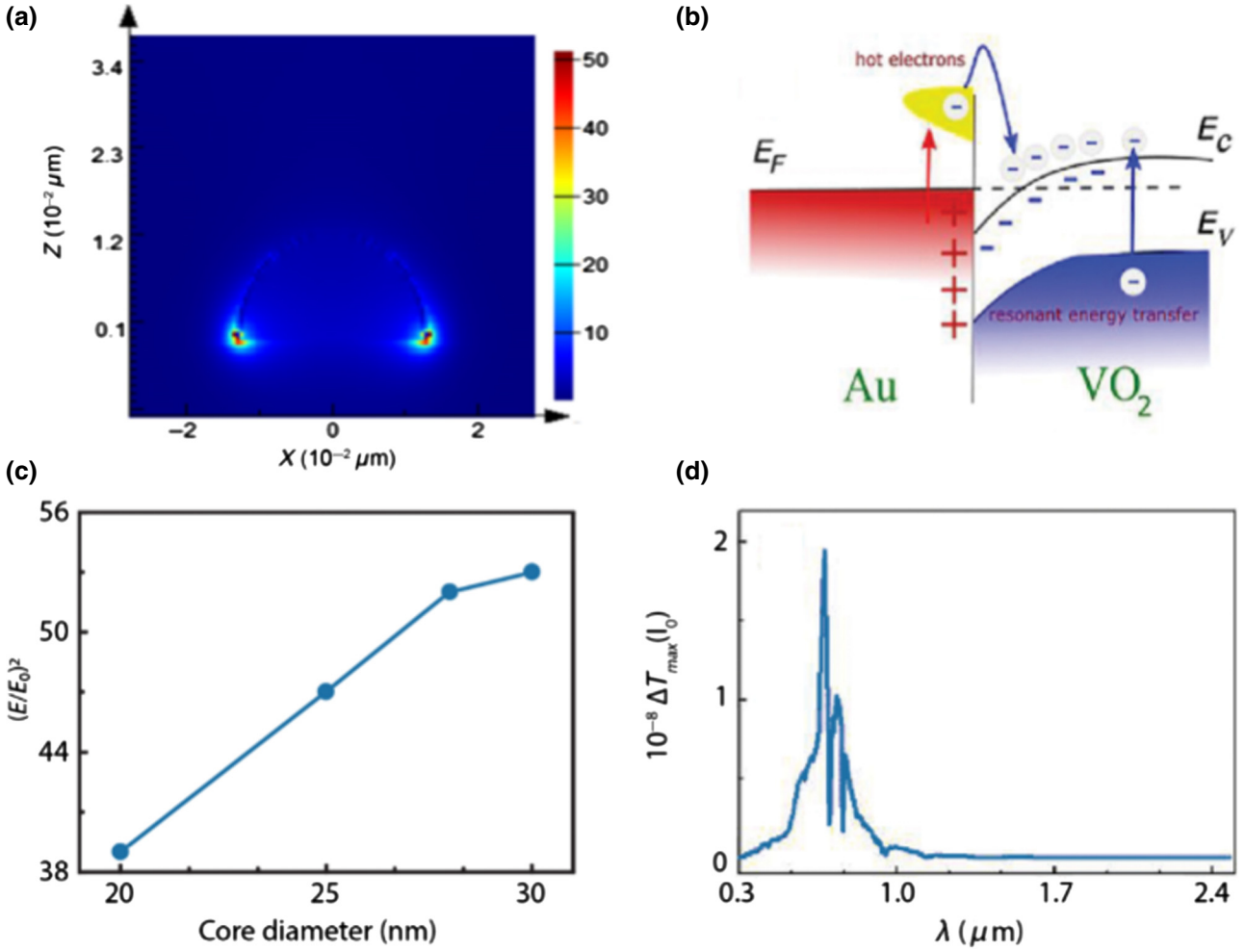

FIG. 5. (a) Normalized field intensity distribution of a composite of Au/VO_2 half sphere (core diameter of 28 nm, coating thickness of 15 nm) at the SPR wavelength = 0.68 μm. (b) Possible mechanisms for charge concentration enhancement following SPR excitation. (c) Maximal field intensity enhancement as a function of Au core diameter. (d) Calculated temperature increase at the surface of Au NP in the VO_2 as a function of wavelength for AM1.5 solar irradiance.

thus formed. The lower electronic work function in Au (4.8 eV) compared to VO_2 (5.4 eV) leads to the electron flow from the Au core to the VO_2 shell [33], which may induce the destabilization of the semiconducting phase. Considering the fact that at the plasmonic resonance the electrons are oscillating with the light field, their high kinetic energy will certainly accelerate their transfer to the semiconductor, and even with slightly low kinetic energy, there is still the possibility of transfer through the quantum tunneling phenomenon [39–41]. The charge density (ρ) of hot carriers generated at the resonance can be evaluated using the classical Gauss law in differential form $\rho = \mathrm{Re}(\varepsilon)\nabla \cdot E$ from the field distribution calculated using the FDTD method. Plasmonic metals such as Au are excellent electrical conductors, hence almost all induced charge is distributed on the Au/VO_2 interface. According to Fig. 5(a), the maximal field enhancement and consequent charge generation is expected at the closest vicinity of the substrate. Figure 5(a) shows the charge distribution around the Au/VO_2 interface of a typical 28-nm diameter composite core/shell nanoparticle, 0.5 nm above the substrate. According to Fig. 6(b), a larger nanoparticle will necessarily generate a larger number of electrons resulting in a larger τ_c decrease. Its larger contact area with the VO_2 surrounding will also help to accelerate the process. Taking into account the broadening of the localized SPR (LSPR) spectrum (600–700 nm range), we estimate the carriers' density of up to approximately 10^{17} electrons/cm^3 available for charge transfer. The lifetime of hot electrons in AuNP is at the same order of magnitude as the metal insulator transition time in VO_2 (hundreds of fs), which explains the low Joule heating temperature enhancement driven by relaxation to phonons (a few ps time frame). The temperature dependence of the electrons' density in VO_2 can be estimated using the formula $n_0(T) \propto T^{3/2}e^{-E_g/2kT}$ where $E_g = 0.6$ eV is the

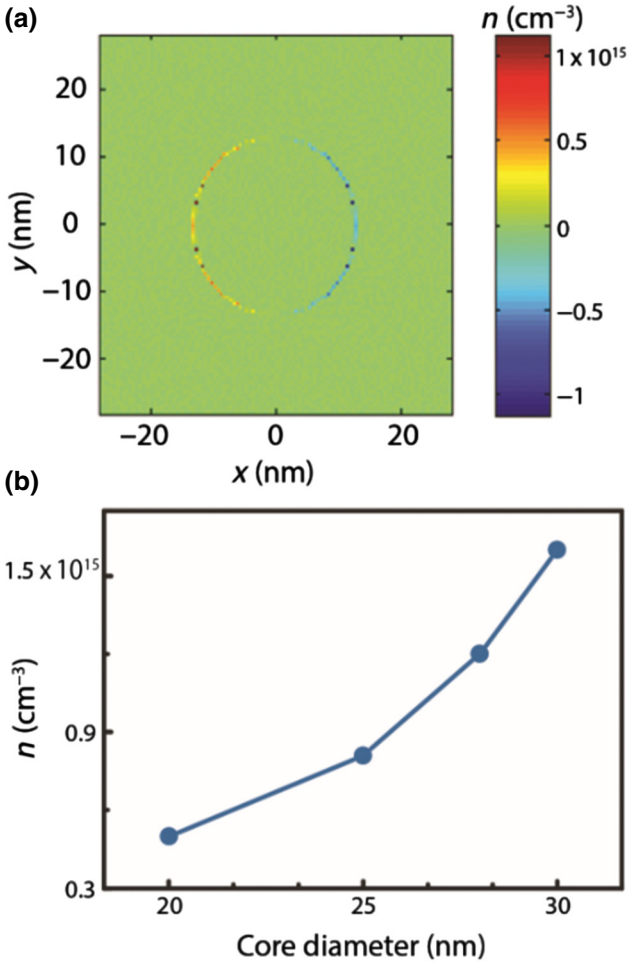

FIG. 6. (a) Charge density of a composite of Au/VO_2 half sphere (core diameter of 28 nm, coating thickness of 15 nm) at the SPR wavelength $\lambda = 0.68$ μm, z = 0.5 nm calculated by Gauss law in differential form. (b) Maximal charge density as a function of Au core diameter. When considering the broad spectrum of the LSPR (600–700 nm), the maximal charge density is expected to reach 10^{17} electrons/cm^3.

band-gap width in the semiconducting phase, and k is the Boltzmann constant [1]. The critical charge density required for the phase transition is on the order of 10^{18} electrons/cm^3, therefore, the charge density for the lowest τ_c obtained experimentally will be 7.5×10^{17} without Au, which is comparable to the highest charge density calculated using the Gauss law applied on an electric field distribution [Fig. 6(b)]. As a result, the excess electrons generated at the LSPR are contributing significantly to the reduction of the τ_c in the Au/VO_2 core/shell configuration. Plasmonic nanoparticles act as efficient light concentrators. In the light concentration mechanism, the NPs' near-field significantly enhances the interband or other optical transitions in the nearby semiconductor if there is an overlap with the LSPR spectra (similar to Förster resonant energy transfer) in what is called a plasmon-induced resonant transfer [42–44]. As with direct light excitation, the charge formation rate in the semiconductor can be obtained from the stationary kinetic equation governing electron generation $n = n_0 f I_0 \tau_R / V E_p$ [45] where f is the quantum efficiency, τ_R is the electron relaxation time, V is the irradiated volume, and E_p is the photon energy. The conduction band width of the relevant allowed energy transition in VO_2 is 2 eV [46], hence the LSPR wavelength of the composite Au/VO_2NP (approximately 1.8 eV) does this and if we can decrease the LSPR wavelength further, we might even reduce the τ_c more. According to Fig. 6(b), the intensity enhancement at the LSPR is expected to provide a factor of 1.4–1.6 in electron density increase at the VO_2 shell, depending on the AuNP core size. As a result, the reduction of τ_c is expected as well if the dominant mechanism is energy transfer through near-field enhancement. Enhancement of photocarriers' generation when plasmonic particles are embedded in a semiconductor is also known to occur due to other mechanisms such as the enhanced scattering and absorption. As the lowering of the τ_c of VO_2 is accompanied with some structural changes according to the Peierls model [47], one can also think of other mechanisms that assist these structural changes to occur with the presence of the hot electrons generated. One of these involves the trapping of the hot electrons in transient traps generated by short-lived large-energy fluctuations and the energy transfer from the hot electrons to the surroundings, thus enhancing the structural phase transitions [48–51].

Based on this, one can think of designs that may improve the lowering of the τ_c even further, for example, by increasing the number of plasmonic resonances within the solar spectrum and using nanoparticles (NPs) or plasmonic antennas that enhance the local field even further [52].

It should be noted that even though we used Bloch boundary conditions for FDTD simulations, the generality of our findings is not supposed to be lost because the actual Au islands are distributed randomly following the deposition process. The main difference between ordered and disordered Au islands' behaviors will be LSPR broadening and random localization of electromagnetic fields in hot spots, which will not change the overall system behavior at the macro scale, in particular for subwavelength periods of the ordered structure.

B. Strain-induced MIT temperature shift

Besides shifting of the τ_c in VO_2 by nonstoichiometry and doping, differences in the τ_c are observed in VO_2 films on different substrates. The reason for this shift is attributed to the existence of thermally induced stresses in thin films due to the differences in the thermal expansion coefficients between film and substrate [10,11,53,54]. The common explanation for strain-induced T_{tr} modification is that the elongation (shrinkage) of the $V^{4+} - V^{4+}$ distance along the c_R axis diminishes (enhances) overlapping

TABLE I. Young's modulus (E), Poisson ratio (υ), and linear thermal expansion coefficient (α) for Au and VO_2.

Material	E (GPa)	υ	α (C^{-1})
Au	78 [56]	0.42 [53]	1.42×10^{-5} [57]
VO_2	140 [58]	0.3 [55]	1.7×10^{-5} [59]

of their d orbitals, thus weakens (strengthens) the metallic R phase [53]. In a similar manner, the thermomechanical stress can be generated in the core–shell nanoparticle configuration due to the difference in the linear thermal expansion coefficients of the core and the shell material [55]. As mentioned in Sec. II A, the VO_2 coating is prepared utilizing the sol-gel method and then annealed at 550 °C. Upon cooling down from the annealing temperature, external stress is developed in the VO_2 shell as a consequence of the thermal expansion mismatch between VO_2 and Au. The radial displacement of the VO_2 shell as a result of the induced stress can be derived from Hook's law in spherical coordinates as Eq. (3) [55]

$$u = r\frac{\varepsilon_{f1}[1-(1-V)(1-\beta)]+\varepsilon_{f2}(1-V)(K_2/K_1)(1-\beta)}{1-[1-(K_2/K_1)](1-V)(1-\beta)} + \frac{\beta r[1+(a/r)^3](\varepsilon_{f2}-\varepsilon_{f1})}{1-[1-(K_2/K_1)](1-V)(1-\beta)}. \quad (3)$$

Here, a is the core radius, ΔT is temperature difference, E_1, E_2 and υ_1, υ_2 are Young's modulus and Poisson ratios of Au and VO_2, respectively, $\beta = 1/3(1+\upsilon_2)/(1-\upsilon_2)$, $K = E/3(1-2\upsilon)$ is a bulk modulus, $\varepsilon_s = (T_{tr} - T_{an})\alpha$ is a free strain, $T_{tr} = 67$ °C is the transition temperature, T_{an} is the annealing (or initial) temperature, and α is the linear thermal expansion coefficient. The temperature is assumed to be uniform throughout the typical thickness of the VO_2 (15 nm) during cooling. According to Table I, the linear thermal expansion coefficient of VO_2 in the metallic phase is larger compared to Au, therefore, a compressive strain is expected to develop in the VO_2 shell. In terms of the radial displacement, u, and the radial coordinate, r, the radial and tangential components of the strain are given by the relations $\varepsilon_r = du/dr$ and $\varepsilon_t = u/r$. The temperature is assumed to be uniform throughout the typical thickness of the VO_2 (15 nm) during cooling. According to Table I, the linear thermal expansion coefficient of VO_2 in the metallic phase is larger compared to Au, therefore, a compressive strain is expected to be developed in the VO_2 shell.

In Fig. 7(a), a typical distribution of strain in the VO_2 shell ($a = 15$ nm) is shown. The strain within the VO_2 shell is position dependent. According to Fig. 7(b), nanocomposites with a larger Au core radius yield larger compressive strain in the VO_2 shell resulting in a lowering of τ_c. Based on this, we conclude that the major contribution for the lowering of τ_c is associated with the strain that

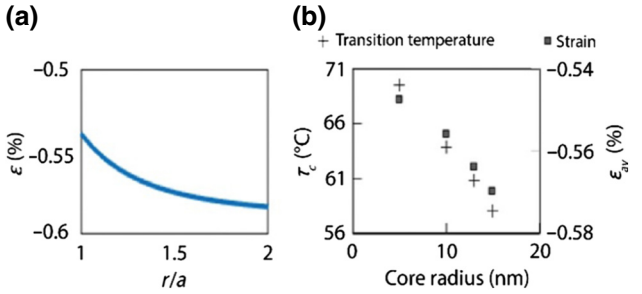

FIG. 7. (a) Radial dependence of strain in VO_2 shell (core radius $r = 15$ nm, coating thickness $a = 15$ nm) calculated by Eq. (2). (b) Influence of core radius on average strain and transition temperature. The squares denote transition temperature and crosses average strain.

appears in a metallic core–shell nanoparticle subjected to the cooling process from the annealing temperature.

Although the plasmon-induced charge transfer and/or generation and local heating are not totally excluded, it seems that at normal irradiation levels and, in our particular case, their contribution, is small compared to the strain-induced reduction of τ_c. Perhaps by focusing the solar radiation, the intensity level will increase by at least an order of magnitude and considering the wide spectral range of plasmon excitation, the plasmon-induced phenomena can become dominant and the reduction of the transition temperature can reach more than 10 °C.

It should be noted that LSPR supported by Au nanoparticles can also modify the color of transmitted or reflected light in a system containing VO_2 nanoparticles, as was shown by Xu *et al.* [34]. In this work, a transition temperature decrease of about 6 °C was demonstrated in a $VO_2/SiO_2/Au$ core/shell nanoparticle configuration having a fixed VO_2 core and SiO_2 interlayer sizes and varying the Au nanoparticles' sizes. The size variation of Au nanoparticles allows continuous tuning of LSPR wavelength, but not the transition temperature reduction τ_c, which remained fixed around 5–7 °C for Au nanoparticles in a 5–21 nm diameter range [34]. For this specific case, it seems that the transition temperature reduction is achieved by the combination of two competing effects – static electron migration through insulating SiO_2 junction and thermal strain at SiO_2/VO_2 interface, which remains constant once there is no variation in the $Au/SiO_2/VO_2$ contact areas. Control of transition temperature by either LSPR or strain-induced effects will occur once the contact area between Au and VO_2 can be controlled directly, for instance, using the Au core/VO_2 shell configuration presented in this work.

C. dc conductivity and percolation-related effects

As the VO_2 phase transition has a wide hysteresis zone, which is a signature of a metal-insulator mix, the MIT in

VO_2 can be considered to be a percolative phase transition. Two component nanostructured networks with one phase metallic and the other insulating undergo a MIT at the critical concentration of metal known as the percolation threshold, where the highly conducting phase first forms a connected network [60]. At first glance, an addition of highly conductive Au nanoparticles into the system under evaluation is supposed to speed up the process of percolating path formation, stabilization of VO_2 metallic phase, and consequent modification of transition temperature τ_c.

In order to evaluate this hypothesis, the produced sample's resistance is measured as a function of temperature using the "Ohms-per-square" method with a four-wire resistance measurement. The measured resistance and dependence of transition temperature and hysteresis on the deposition time are shown in Figs. 8(a) and 8(b), respectively. The electrical transition temperature and hysteresis width are calculated using the same procedure as for the optical measurements. It can be seen that the electrical switching temperature remains approximately constant with the increment of the Au core size, whereas the hysteresis width follows the same tendency as observed for the optical measurements. The offset between the effective optical and electrical switching temperatures arises because the hysteresis in optical transmissivity is determined by the relative fraction of nanoparticles in the semiconducting state, while the hysteresis in electrical resistivity is governed by the evolution of a continuous percolation path during the heating process or extinction of the percolation path during the cooling process [61]. The significant decrease of resistivity at deposition times of 100 and 120 s throughout the whole temperature range of our experiment indicates that the Au volume fraction crosses the percolation threshold [see Fig. 8(c) for details]. Nevertheless, the contribution of this effect to the transition temperature modification is not observed. Two main characteristic features can be identified in the measured resistance curves:

(i) The simultaneous electrical hysteresis width increase and multiple branches appearance at high deposition times of Au could be associated with the increasing nonuniformity of the Au/VO_2 core/shell NPs distribution as the deposition time of Au grows [see Figs. 2(c) and 2(d) for details] [62].

(ii) The form of the thermal hysteresis between the heating branch and the cooling branch is asymmetric for all deposition times. This phenomenon is attributed to the difference in the metallic domains distribution variation in the heating cycle compared to the cooling cycle of the experiment [63]. VO_2 exists in two distinct phases, a low-temperature insulator phase where it possesses a monoclinic structure, and a high-temperature metallic phase with a tetragonal rutile structure. At intermediate temperature, VO_2 exists as a mixture of the two constituent phases and its properties could be described using the effective medium theory (EMT). Such a mixture could be parameterized using the filling fraction [61] (f) which represents the fraction of the material existing in the metallic phase, that is, f is 0 and 1 for the insulator and metallic phases, respectively, and f is between 0 and 1 while the material is undergoing the transition.

To the first approximation, the optical transmittance depends linearly on the volume fraction of the metallic phase [59]. We use the volume fraction values obtained from optical data in order to map it onto the resistivity data at each temperature to obtain a plot of resistivity as a function of volume fraction. The results for the cooling cycle are shown in Fig. 8(d). A clear tendency of critical volume fraction increase is observed from $f = 0.19$ for 60 seconds deposition time to $f = 0.33$ for 12 seconds deposition time.

These phenomena can be attributed to the increase of the energy barrier that the isolating domains of VO_2 have to overcome to show up within the metallic matrix of both Au and VO_2 in the cooling process [64].

EMT has been applied for the description of various properties of the semiconductor-metal transition in VO_2 such as optical transmission [65,66], electrical conductivity, and heat capacity [64]. We employ the EMT for modeling of the Au/VO_2 core/shell NPs' resistance in three steps:

(i) The conductivity of VO_2 is calculated using the 2D version of Bruggeman EMT and assuming that the semiconducting/metallic inclusions are spherical [67]

$$\sigma_{VO_2} = \frac{1}{4}\left(\beta + \sqrt{\beta^2 + 8\sigma_s\sigma_m}\right), \tag{4}$$

where $\beta = (3\sigma_m - 1)f + (3\sigma_i - 1)(1-f)$, $\sigma_{i,m}$ stands for the conductivity of VO_2 in semiconducting and metallic phases, respectively, and the fill volume fraction f is extracted from the optical measurements.

(ii) The effective conductivity of the core-shell structure is calculated using the internal homogenization approach developed by Chettiar *et al.* [68]

$$\sigma_{\text{eff}} = \sigma_{VO_2}\frac{b^3(\sigma_{Au} + 2\sigma_{VO_2}) + 2a^3(\sigma_{Au} - \sigma_{VO_2})}{b^3(\sigma_{Au} + 2\sigma_{VO_2}) - a^3(\sigma_{Au} - \sigma_{VO_2})}. \tag{5}$$

Here, σ_{Au} is the gold conductivity and a and b are inner and outer radii of the Au/VO_2 core/shell NP.

(iii) Finally, the resistivity is calculated as the reciprocal of the effective conductivity.

The simulated resistance and dependence of transition temperature and hysteresis on the deposition time are shown in Figs. 8(e) and 8(f), respectively. Several important differences can be identified once the experimental resistivity

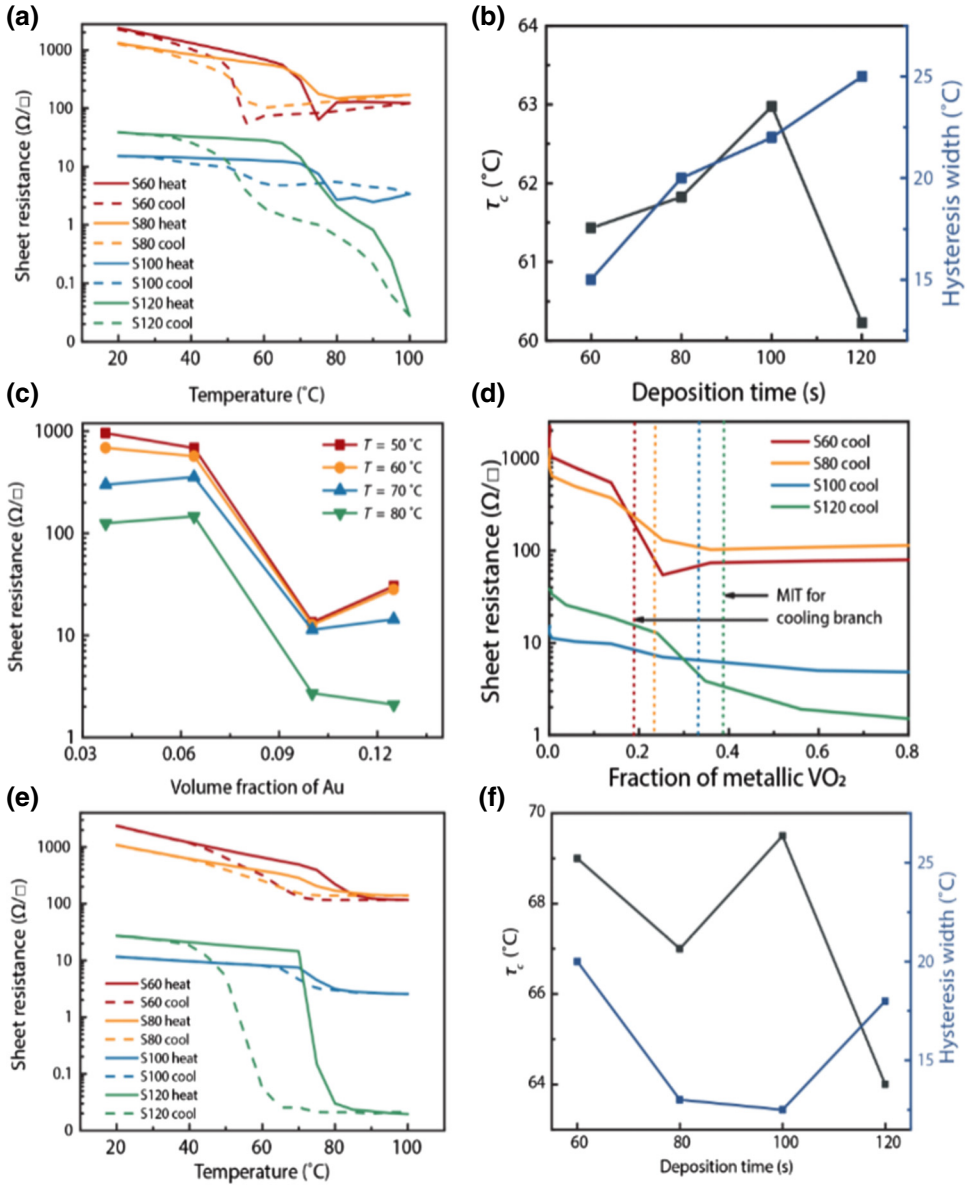

FIG. 8. (a) Measured sheet resistivity of Au/VO_2 composite with various deposition times from 60 to 120 s. (b) Transition temperature and hysteresis calculated using the experimental data. (c) Sheet resistance temperature slices as a function of volume fraction of Au at the vicinity of τ_c. (d) Sheet resistance of the cooling cycle as a function of the volume fraction of VO_2 in the metallic phase. The MIT is denoted by vertical lines. (e) Sheet resistivity calculated using Bruggeman formalism and homogenization approach. (f) Transition temperature and hysteresis calculated using simulated data.

transition temperature and hysteresis width results shown in Fig. 8(b) are compared to the simulated results shown in Fig. 8(f). Essentially, the transition temperature of the simulated results remains constant around 70 °C with a sharp drop for the deposition time of 120 s. The constant positive offset between the simulated and experimental transition temperatures can be attributed to the intrinsic strain, which is induced at the VO_2 shell. This factor is not taken into account in either the Bruggeman or internal homogenization models used for calculation of the Au/VO_2 core/shell NP resistance. The hysteresis width of simulated data remains approximately constant at all deposition times. The proper evaluation of hysteresis width requires consideration of both semiconducting and metallic domains and the Au/VO_2 NP distribution [62] and shape variation [69], proper evaluation of the VO_2 phase domains energy creation, and so on, factors that are hard to control experimentally and challenging to consider in a theoretical modeling process.

To summarize, the addition of Au into the VO_2 percolating system is not identified as a dominant factor for transition temperature modification in the electrical domain. Transition temperature modification occurs in the optical domain only and is preliminarily controlled by the

ratio between the semiconducting and metallic volume fractions, which varies as a result of the intrinsic strain developed on the core/shell interface.

IV. CONCLUSIONS

In this work, Au half spheres that support localized plasmons are embedded within thermochromic VO_2 thin film to form the VO_2/Au half-sphere core-shell structure. The plasmon resonance wavelength and thermochromic properties of this structure show a strong dependence on the Au deposition thickness. A larger Au core gives rise to a redshift and broadening of the resonance peak for both the semiconductor phase and metal phase. By varying this parameter, the resonance wavelength (λ_{SPR}) of the Rutile phase can be regulated from 600 to 720 nm. τ_c is reduced by approximately 10 °C with the increase of Au core size. The simulation results suggest that the local photothermal effects can be important only when the solar energy is concentrated. The three main mechanisms of hot electrons transfer due to plasma oscillation, due to photocarriers generation, or due to local heating are found not to contribute significantly to the observed τ_c reduction under normal irradiation levels. These three mechanisms can be significant at higher irradiation levels or when the plasmonic enhancement is much larger. They might occur simultaneously so that one needs to solve the problem in a more rigorous way by taking into account the coupling between the different mechanisms. The major contributing factor for the transition temperature reduction is associated with the induced thermal strain at the surface of the AuNPs that appear in the system due to the cooling step in the annealing process. The stabilization of the metallic phase occurring as a result of induced strain does not introduce a significant change in the percolation path formation of VO_2 regardless of Au core size variation. Our results are specific to VO_2, yet are universally relatable to other correlated electron materials. Further designs and experimental works are planned to clarify the role of the strains vs plasmonic effects depending on the type, shape, and size of the nanoparticles. It is believed that this research will lead to the creation of an optimized thermochromic material with the desired transition temperature without sacrificing its properties for switching devices, optical waveguides, optical limiting elements, sensing components, tunable metamaterials, and smart window applications.

ACKNOWLEDGMENTS

This research is supported by grants from the National Research Foundation, Prime Minister's Office, Singapore under its Campus of Research Excellence and Technological Enterprise (CREATE) programme.

[1] A. Zylbersztejn and N. F. Mott, Metal-insulator transition in vanadium dioxide, Phys. Rev. B **11**, 4383 (1975).
[2] F. Morin, Oxides Which Show a Metal-to-Insulator Transition at the Neel Temperature, Phys. Rev. Lett. **3**, 34 (1959).
[3] C. G. Granqvist, transparent conductors as solar energy materials: A panoramic review, Sol. Energy Mater. Sol. Cells **91**, 1529 (2007).
[4] S. Chen, H. Ma, X. Yi, H. Wang, X. Tao, M. Chen, X. Li, and C. Ke, Optical switch based on vanadium dioxide thin films, Inf. Phys. Technol. **45**, 239 (2004).
[5] T. Driscoll, H. T. Kim, B. G. Chae, B. J. Kim, Y. W. Lee, N. M. Jokerst, S. Palit, D. R. Smith, M. Di Ventra, and D. N. Basov, Memory metamaterials, Science **325**, 1518 (2009).
[6] H. Futaki and M. Aoki, Effects of various doping elements on the transition temperature of vanadium oxide semiconductors, Jpn. J. Appl. Phys. **8**, 1008 (1969).
[7] S. Wang, K. A. Owusu, L. Mai, Y. Ke, Y. Zhou, P. Hu, S. Magdassi, and Y. Long, Vanadium dioxide for energy conservation and energy storage applications: Synthesis and performance improvement, Appl. Energy **211**, 200 (2018).
[8] W. Burkhardt, T. Christmann, B. Meyer, W. Niessner, D. Schalch, and A. Scharmann, W- and F-doped VO_2 films studied by photoelectron spectrometry, Thin Solid Films **345**, 229 (1999).
[9] T. Hanlon, J. Coath, and M. Richardson, Molybdenum-doped vanadium dioxide coatings on glass produced by the aqueous Sol–Gel method, Thin Solid Films **436**, 269 (2003).
[10] F. C. Case, Modifications in the phase transition properties of predeposited VO_2 films, J. Vac. Sci. Technol. A **2**, 1509 (1984).
[11] K. D. Ufert, Stress induced switching in VO_2 thin films, Phys. Status Solidi A **34**, K83 (1976).
[12] A. Cavalleri, T. Dekorsy, H. H. W. Chong, J.-C. Kieffer, and R. W. Schoenlein, Evidence for a structurally-driven insulator-to-metal transition in VO_2: A view from the ultrafast timescale, Phys. Rev. B **70**, 161102 (2004).
[13] M. Liu, H. Y. Hwang, H. Tao, A. C. Strikwerda, K. Fan, G. R. Keiser, A. J. Sternbach, K. G. West, S. Kittiwatanakul, and J. Lu, Terahertz-field-induced insulator-to-metal transition in vanadium dioxide metamaterial, Nature **487**, 345 (2012).
[14] G. Stefanovich, A. Pergament, and D. Stefanovich, Electrical switching and mott transition in VO_2, J. Phys.: Condens. Matter **12**, 8837 (2000).
[15] M. Nakano, K. Shibuya, D. Okuyama, T. Hatano, S. Ono, M. Kawasaki, Y. Iwasa, and Y. Tokura, Collective bulk carrier delocalization driven by electrostatic surface charge accumulation, Nature **487**, 459 (2012).
[16] N. Wang, M. Duchamp, C. Xue, R. E. Dunin-Borkowski, G. Liu, and Y. Long, Single-crystalline W-doped VO_2 nanobeams with highly reversible electrical and plasmonic responses near room temperature, Adv. Mater. Interfaces **3**, 1600164 (2016).
[17] Y. Ke, X. Wen, D. Zhao, R. Che, Q. Xiong, and Y. Long, Controllable fabrication of two-dimensional patterned VO_2

nanoparticle, nanodome, and nanonet arrays with tunable temperature-dependent localized surface plasmon resonance, ACS Nano **11**, 7542 (2017).
[18] M. Maaza, O. Nemraoui, C. Sella, and A. Beye, Surface plasmon resonance tunability in Au − VO_2 thermochromic nano-composites, Gold Bull. **38**, 100 (2005).
[19] M. Yi, C. Lu, Y. Gong, Z. Qi, and Y. Cui, Dual-functional sensor based on switchable plasmonic structure of VO_2 nano-crystal films and Ag nanoparticles, Opt. Express **22**, 29627 (2014).
[20] A. Joushaghani, B. A. Kruger, S. Paradis, D. Alain, J. Stewart Aitchison, and J. K. Poon, Wavelength-size hybrid Si-VO_2 waveguide electroabsorption optical switches and photodetectors, Appl. Phys. Lett. **102**, 061101 (2013).
[21] D. W. Ferrara, J. Nag, E. R. MacQuarrie, A. B. Kaye, and R. F. Haglund, Jr., Plasmonic probe of the semiconductor to metal phase transition in vanadium dioxide, Nano Lett. **13**, 4169 (2013).
[22] G. Xu, C.-M. Huang, M. Tazawa, P. Jin, and L.-H. Chen, Tunable optical pproperties of nano-Au on vanadium dioxide, Opt. Commun. **282**, 896 (2009).
[23] H. Zhou, X. Cao, M. Jiang, S. Bao, and P. Jin, Surface plasmon resonance tunability in VO_2/Au/VO_2 thermochromic structure, Laser Photonics Rev. **8**, 617 (2014).
[24] D. Ferrara, E. MacQuarrie, J. Nag, A. Kaye, and R. Haglund, Jr., Plasmon-enhanced low-intensity laser switching of gold: Vanadium dioxide nanocomposites, Appl. Phys. Lett. **98**, 241112 (2011).
[25] K. Appavoo, B. Wang, N. F. Brady, M. Seo, J. Nag, R. P. Prasankumar, D. J. Hilton, S. T. Pantelides, and R. F. Haglund, Jr., Ultrafast phase transition via catastrophic phonon collapse driven by plasmonic hot-electron injection, Nano Lett. **14**, 1127 (2014).
[26] X. Qian, N. Wang, Y. Li, J. Zhang, Z. Xu, and Y. Long, Bioinspired multifunctional vanadium dioxide: Improved thermochromism and hydrophobicity, Langmuir **30**, 10766 (2014).
[27] Y. Ke, I. Balin, N. Wang, Q. Lu, L. Y. A. Tok, T. J. White, S. Magdassi, I. Abdulhalim, and Y. Long, Two-dimensional SiO_2/VO_2 photonic crystals with statically visible and dynamically infrared modulated for smart window deployment, ACS Appl. Mater. Interfaces **8**, 33112 (2016).
[28] Q. Lu, C. Liu, N. Wang, S. Magdassi, D. Mandler, and Y. Long, Periodic micro-patterned VO_2 thermochromic films by mesh printing, J. Mater. Chem. C **4**, 8385 (2016).
[29] G. Wyszecki and W. S. Stiles, *Color Science: Concepts and Methods, Quantitative Data and Formulas* (John Wiley & Sons, Inc., London, 1967).
[30] A. S. T. M., *G173-03 Standard Tables of Reference Solar Spectral Irradiances: Direct Normal and Hemispherical on a 37 Tilted Surface, in Annual Book of ASTM Standards American Society for Testing and Materials* (ASTM, Philadelphia, PA, USA, 2003).
[31] C. Liu, Y. Long, S. Magdassi, and D. Mandler, Ionic strength induced electrodeposition: A universal approach for nanomaterial deposition at selective areas, Nanoscale **9**, 485 (2017).
[32] G. Xu, C.-M. Huang, M. Tazawa, P. Jin, D.-M. Chen, and L. Miao, Electron injection assisted phase transition in a nano-Au-VO_2 junction, Appl. Phys. Lett. **93**, 061911 (2008).
[33] J.-C. Orlianges, J. Leroy, A. Crunteanu, R. Mayet, P. Carles, and C. Champeaux, Electrical and optical properties of vanadium dioxide containing gold nanoparticles deposited by pulsed laser deposition, Appl. Phys. Lett. **101**, 133102 (2012).
[34] X. Lu, X. Xiao, Z. Cao, Y. Zhan, H. Cheng, and G. Xu, A novel method to modify the color of VO_2-Based thermochromic smart films by solution-processed VO_2@SiO_2@Au core–shell nanoparticles, RCS Adv. **6**, 47249 (2016).
[35] A. I. Maaroof, D. Cho, B. Kim, H. Kim, and S. C. Hong, Hybrid nanostructures based on VO_2 semishells and Au nanohemispheres for tunable plasmonic coupling, J. Phys. Chem. C **117**, 19601 (2013).
[36] A. O. Govorov, W. Zhang, T. Skeini, H. Richardson, J. Lee, and N. A. Kotov, Gold nanoparticle ensembles as heaters and actuators: melting and collective plasmon resonances, Nanoscale Res. Lett. **1**, 84 (2006).
[37] D.-W. Oh, C. Ko, S. Ramanathan, and D. G. Cahill, Thermal conductivity and dynamic heat capacity across the metal-insulator transition in thin film VO_2, Appl. Phys. Lett. **96**, 151906 (2010).
[38] C. Berglund and H. Guggenheim, Electronic properties of VO_2 near the semiconductor-metal transition, Phys. Rev. **185**, 1022 (1969).
[39] K. J. Savage, M. M. Hawkeye, R. Esteban, A. G. Borisov, J. Aizpurua, and J. J. Baumberg, Revealing the quantum regime in tunneling plasmonics, Nature **491**, 574 (2012).
[40] W. Zhu, R. Esteban, A. G. Borisov, J. J. Baumberg, P. Nordlander, H. J. Lezec, J. Aizpurua, and K. B. Crozier, Quantum mechanical effects in plasmonic structures with subnanometre gaps, Nat. Commun. **7**, 11495 (2016).
[41] D. C. Marinica, M. Zapata, P. Nordlander, A. K. Kazansky, P. M. Echenique, J. Aizpurua, and A. G. Borisov, Active quantum plasmonics, Sci. Adv. **1**, e1501095 (2015).
[42] L.-Y. Hsu, W. Ding, and G. C. Schatz, Plasmon-coupled resonance energy transfer, J. Phys. Chem. Lett. **8**, 2357 (2017).
[43] G. L. Liu, Y.-T. Long, Y. Choi, T. Kang, and L. P. Lee, Quantized plasmon quenching dips nanospectroscopy via plasmon resonance energy transfer, Nat. Methods **4**, 1015 (2007).
[44] J. Li, S. K. Cushing, F. Meng, T. R. Senty, A. D. Bristow, and N. Wu, Plasmon-induced resonance energy transfer for solar energy conversion, Nat. Photonics **9**, 601 (2015).
[45] I. Abdulhalim, R. Beserman, and Y. L. Khait, Laser-induced oscillatory instabilities in amorphous materials, EPL **4**, 1371 (1987).
[46] M. M. Qazilbash, A. A. Schafgans, K. S. Burch, S. J. Yun, B. G. Chae, B. J. Kim, H. T. Kim, and D. N. Basov, Electrodynamics of the vanadium oxides VO_2 and V_2O_3, Phys. Rev. B **77**, 115121 (2008).
[47] J. B. Goodenough, The two components of the crystallographic transition in VO_2, J. Solid State Chem. **3**, 490 (1971).
[48] I. Abdulhalim, Model for photoinduced defects and photorefractivity in optical fibers, Appl. Phys. Lett. **66**, 3248 (1995).
[49] I. Abdulhalim, Kinetic model for photoinduced and thermally induced creation and annihilation of metastable

defects in hydrogenated amorphous silicon, J. Appl. Phys. **77**, 1897 (1995).

[50] I. Abdulhalim, R. Beserman, and R. Weil, Structural changes and crystallization of amorphous hydrogenated silicon generated by laser irradiation, Phys. Rev. B: Solid State **39**, 1081 (1989).

[51] I. Abdulhalim, R. Beserman, and R. Weil, Photodarkening, structural instabilities, and crystallization of glassy As_2Se_3 induced by laser irradiation, Phys. Rev. B: Solid State **40**, 12476 (1989).

[52] M. Abutoama, S. Li, and I. Abdulhalim, Widening the spectral range of ultrahigh field enhancement by efficient coupling of localized to extended plasmons and cavity resonances in grating geometry, J. Phys. Chem. C **121**, 27612 (2017).

[53] Y. Muraoka and Z. Hiroi, Metal–insulator transition of VO_2 thin films grown on TiO_2 (001) and (110) substrates, Appl. Phys. Lett. **80**, 583 (2002).

[54] J. Sakai, M. Zaghrioui, M. Matsushima, H. Funakubo, and K. Okimura, Impact of thermal expansion of substrates on phase transition temperature of VO_2 films, J. Appl. Phys. **116**, 123510 (2014).

[55] G. W. Scherer, Viscoelastic analysis of thermal stresses in a composite sphere, J. Am. Ceram. Soc. **66**, 59 (1983).

[56] J. R. Partington, Tables of physical and chemical constants: and some mathematical functions. By G. W. C. Kaye and T. H. Laby, J. Phys. Chem. **40**, 938 (1935).

[57] Y. S. Touloukian and C. Ho, eds., *Thermophysical Properties of Matter - the TPRC Data Series* (IFI/Plenum, New York, 1970).

[58] Y. Gu, J. Cao, J. Wu, and L.-Q. Chen, Thermodynamics of strained vanadium dioxide single crystals, J. Appl. Phys. **108**, 083517 (2010).

[59] T. Kawakubo and T. Nakagawa, Phase transition in VO_2, J. Phys. Soc. Jpn **19**, 517 (1964).

[60] L. A. L. de Almeida, G. S. Deep, A. M. N. Lima, I. A. Khrebtov, V. G. Malyarov, and H. Neff, Modeling and performance of vanadium–oxide transition edge microbolometers, Appl. Phys. Lett. **85**, 3605 (2004).

[61] J. Rozen, R. Lopez, R. F. Haglund, Jr., and L. C. Feldman, Two-dimensional current percolation in nanocrystalline vanadium dioxide films, Appl. Phys. Lett. **88**, 081902 (2006).

[62] V. A. Klimov, I. O. Timofeeva, S. D. Khanin, E. B. Shadrin, A. V. Ilinski, and F. Silva-Anrade, Hysteresis loop construction for the metal-semiconductor phase transition in vanadium dioxide films, Tech. Phys. **47**, 1134 (2002).

[63] C. O. F. Ba, F. Fortin, S. T. Ba, and R. Valee, Formation of VO_2 by rapid thermal annealing and cooling of sputtered vanadium thin films, J. Vac. Sci. Technol. A **34**, 031505 (2016).

[64] J. Ordonez-Miranda, Y. Ezzahri, K. Joulain, J. Drevillon, and J. J. Alvarado-Gil, Modeling of the electrical conductivity, thermal conductivity, and specific heat capacity of VO_2, Phys. Rev. B **98**, 075144 (2018).

[65] H. S. Choi, J. S. Ahn, J. H. Jung, T. W. Noh, and D. H. Kim, Mid-infrared properties of VO_2 film near the metal-insulator transition, Phys. Rev. B **54**, 4621 (1996).

[66] P. U. Jepsen, B. M. Fischer, A. Thoman, H. Helm, J. Y. Suh, R. Lopez, and R. F. Haglund, Jr., Metal-insulator phase transition in VO_2 thin film observed with terahertz spectroscopy, Phys. Rev. B **74**, 205103 (2006).

[67] D. A. G. Bruggeman, Berechnung Verschiedener Physikalischer Konstanten von Heterogenen Substanzen. I. Dielektrizitätskonstanten und Leitfähigkeiten der Mischkörper aus isotropen Substanzen, Ann. Phys. **24**, 636 (1935).

[68] U. K. Chettiar and N. Engheta, Internal homogenization: Effective permittivity of a coated sphere, Opt. Express **20**, 22976 (2012).

[69] I. Voloshenko, F. Kuhl, B. Gompf, A. Polity, G. Schnoering, A. Berrier, and M. Dressel, Microscopic nature of the asymmetric hysteresis in the insulator-metal transition of VO_2 revealed by spectroscopic ellipsometry, Appl. Phys. Lett. **113**, 201906 (2018).